Title

Paleomagnetism and Paleosecular Variations From the Plio-Pleistocene Golan Heights Volcanic Plateau, Israel

Journal

Geochemistry, Geophysics, Geosystems, 20(9)

ISSN

1525-2027

Authors

Behar, Nicole
Shaar, Ron
Tauxe, Lisa
et al.

Publication Date

2019-09-01

DOI

10.1029/2019gc008479

Peer reviewed

Geochemistry, Geophysics, Geosystems

RESEARCH ARTICLE
10.1029/2019GC008479

Key Points:
- Paleomagnetic data from 91 Plio-Pleistocene lava flows from the Golan Heights (GH) volcanic plateau (32–33°N), Israel
- The GH paleomagnetic pole is in agreement with a GAD field, and the averaged inclination anomaly is nearly zero
- We reevaluate the latitudinal dependency of inclination anomaly from the PSV10 global database using different selection criteria and calculation methods

Supporting Information:
- Supporting Information S1
- Table S3

Correspondence to:
N. Behar,
nicole.behar@mail.huji.ac.il

Citation:
Behar, N., Shaar, R., Tauxe, L., Asefaw, H., Ebert, Y., Heimann, A., et al. (2019). Paleomagnetism and paleosecular variations from the Plio-Pleistocene Golan Heights volcanic plateau, Israel. *Geochemistry, Geophysics, Geosystems*, *20*, 4319–4335. https://doi.org/10.1029/2019GC008479

Received 3 JUN 2019
Accepted 8 AUG 2019
Accepted article online 13 AUG 2019

Paleomagnetism and Paleosecular Variations From the Plio-Pleistocene Golan Heights Volcanic Plateau, Israel

Nicole Behar[1], Ron Shaar[1], Lisa Tauxe[2], Hanna Asefaw[2], Yael Ebert[1], Ariel Heimann[3], Anthony A. P. Koppers[4], and Hagai Ron[1,5]

[1]The Institute of Earth Sciences, Hebrew University of Jerusalem, Jerusalem, Israel, [2]Scripps Institution of Oceanography, University of California San Diego, La Jolla, CA, USA, [3]Geological Survey of Israel, Jerusalem, Israel, [4]College of Earth, Ocean and Atmospheric Sciences, Oregon State University, Corvallis, OR, USA, [5](1944–2012)

Abstract Statistical analysis of geomagnetic paleosecular variation (PSV) and time-averaged field has been largely based on global compilations of paleomagnetic data from lava flows. These show different trends in the averaged inclination anomaly (ΔI) between the two hemispheres, with small positive (<2°) anomalies in midsouthern latitudes and large negative (> −5°) anomalies in midnorthern latitudes. To inspect the large ΔI between 20°N and 40°N we augment the global data with a new paleomagnetic data set from the Golan-Heights (GH), a Plio-Pleistocene volcanic plateau in northeast Israel, located at 32–33°N. The GH data set consists of 91 lava flows sites: 40 sites obtained in the 1990s and 51 obtained in this study. The chronology of the flows is constrained by 57 $^{40}Ar/^{39}Ar$ ages: 39 from previous studies and 18 from this study, which together cover most of the GH plateau. We show that the 1990s data set might be affected by block rotations and does not fully sample PSV. The Plio-Pleistocene pole (86.3°N, 120.8°E, $N = 44$, $k = 25$, $\alpha_{95} = 4.4°$), calculated after applying selection criteria with Fisher precision parameter (k) ≥ 100 and number of specimens per site (n) ≥ 5 is consistent with a geocentric axial dipole field and shows smaller inclination anomaly ($\Delta I = -0.4°$) than predicted by global compilations and PSV models. Reexamination of the inclination anomaly in the global compilation using different calculation methods and selection criteria suggests that inclination anomaly values are affected by (1) inclusion of poor quality data, (2) averaging data by latitude bins, and (3) the way the inclination anomaly is calculated.

Plain Language Summary Since the early days of paleomagnetic research it has been inferred that the time-averaged structure of the field is a geocentric axial dipole (GAD)—equivalent to a field generated by a dipole at the center of the Earth aligned with its rotation axis. This so-called GAD hypothesis is fundamental in paleomagnetism and is the basis for plate tectonic reconstructions. However, recent studies have suggested persistent departures from a GAD structure, manifested as an anomaly in the inclination angle of the field in northern hemispheric low to middle latitudes. To address this problem, we analyzed 91 basaltic lava flows from the Golan Heights volcanic plateau in Israel (32–33°N), spanning the past 5 Myr. As each basaltic flow captured the direction of the ambient magnetic field when it cooled, these flows provide us information about the averaged direction of the ancient geomagnetic field. Our results show that the averaged field in the Golan Heights is in agreement with a GAD structure. We also show that if we reanalyze the global paleomagnetic data from lava flows spanning the past 10 Myr using stricter selection criteria and a different inclination anomaly calculation method, the data do not support a global non-GAD field.

1. Introduction

One of the most fundamental assumptions in paleomagnetism is that the time-averaged geomagnetic field can be approximated by a geocentric axial dipole (GAD). The GAD assumption is the basis for paleomagnetic applications in tectonics and is central in geodynamo modeling. Yet, departures of the time-averaged field (TAF) from a simple GAD field model have been suggested since the 1970s (Cromwell et al., 2018; Johnson et al., 2008; Johnson & Constable, 1996; Lee, 1983; McElhinny & McFadden, 1997; McElhinny & Merrill, 1975; Quidelleur et al., 1994; Wilson, 1970). The details concerning the nondipole components in the TAF have remained elusive, such as whether they are real or an artifact, permanent or vary with time and the role of nonzonal contributions (Johnson & McFadden, 2015).

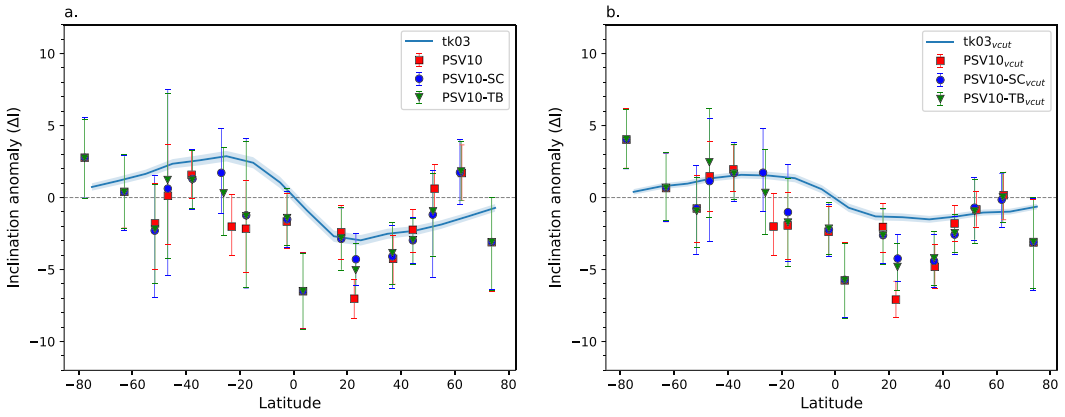

Figure 1. Averaged inclination anomaly (ΔI) versus latitude calculated following Cromwell et al. (2018). ΔIs are calculated from a mean of paleomagnetic directions within 10° latitude bins using six subsets of PSV10 compilation (see Cromwell et al., 2018 for details). (a) All data in PSV10 compilations. (b) Same as (a) but excluding excursional sites using the Vandamme method (Vandamme, 1994). Solid line shows bootstrap means and 95% confidence intervals calculated from 10,000 directions for each bin drawn from TK03.GAD field model (Tauxe & Kent, 2004), where in (b) excursional directions in each bin are removed following Vandamme (1994).

Statistical analysis of the TAF has been largely based on global compilations of paleomagnetic data from lava flows (e.g., Cromwell et al., 2018; Johnson et al., 2008; Johnson & McFadden, 2015; McElhinny & McFadden, 1997). Lava flows are a fundamental source of information because they provide instantaneous recordings of the ancient geomagnetic field at the time the lava cooled. Since the spatial and temporal coverage of lava flows is limited, statistical treatments are required to derive a global description of the TAF. One of the frequently used statistics in TAF analysis is the inclination anomaly ($\Delta I = \bar{I}_{\mathrm{measured}} - I_{\mathrm{GAD}}$), which is a measure of the deviation of the averaged paleomagnetic vector from the expected GAD inclination. Caution should be taken when interpreting inclination anomaly data as a TAF feature because $\bar{I}_{\mathrm{measured}}$ is traditionally calculated by averaging unit vectors. This leads to negative ΔI in the Northern Hemisphere and positive ΔI in the Southern Hemisphere where the magnitude of this bias depends on the statistical properties of paleomagnetic secular variation (PSV; Creer, 1983; Johnson et al., 2008). Figure 1 shows inclination anomalies calculated by Cromwell et al. (2018) from the PSV10 compilation—the latest compilation of lava flows (Cromwell et al., 2018). The inclination anomalies, calculated by averaging paleomagnetic directions in 10° latitude bins, show asymmetry between hemispheres manifested as small positive (<2°) anomalies in midsouthern latitudes and small negative (< −2°) anomalies in low-southern latitudes in contrast to large negative (> −5°) anomalies in midnorthern latitudes and an aberrant low anomaly in 0–10°N latitude bin. To explore whether this behavior is an artifact caused by low-quality data, insufficient data, or by the method through which the averaged inclination anomaly is calculated, additional high-quality data, especially from midlatitude locations, is required. Here, we augment the global PSV data with a new high-quality data set from an undersampled region in midnorthern latitudes in order to examine the large negative ΔI trend between 20°N and 40°N shown in Figure 1. To this end, we conducted a detailed paleomagnetic study in the Golan Heights (GH), a basaltic Plio-Pleistocene volcanic plateau located at latitudes 32–33°N, Israel.

2. Study Area

The GH, located in northeastern Israel (32.6–33.2°N, 35.6–35.9°E), is a Plio-Pleistocene volcanic plateau that constitutes the western edge of the large Cenozoic Harrat Ash-Shaam volcanic field (Figure 2). The GH volcanic sequence comprises mainly lava flows and cinder cones within the alkali basalt-hawaiite-basanite composition spectrum (Weinstein et al., 2006). The GH area was mapped at a 1:50,000 scale by Michelson and Mor (1985) and Mor (1986, 1987a, 1987b) based on morphologic criteria and a few tens of K-Ar dates. Sneh and Weinberger (2003, 2006) provided a revision to the 1:50,000 maps of the northwestern GH. Recent studies provided higher-resolution maps of some confined areas (Shaanan et al., 2010; Weinstein et al., 2013).

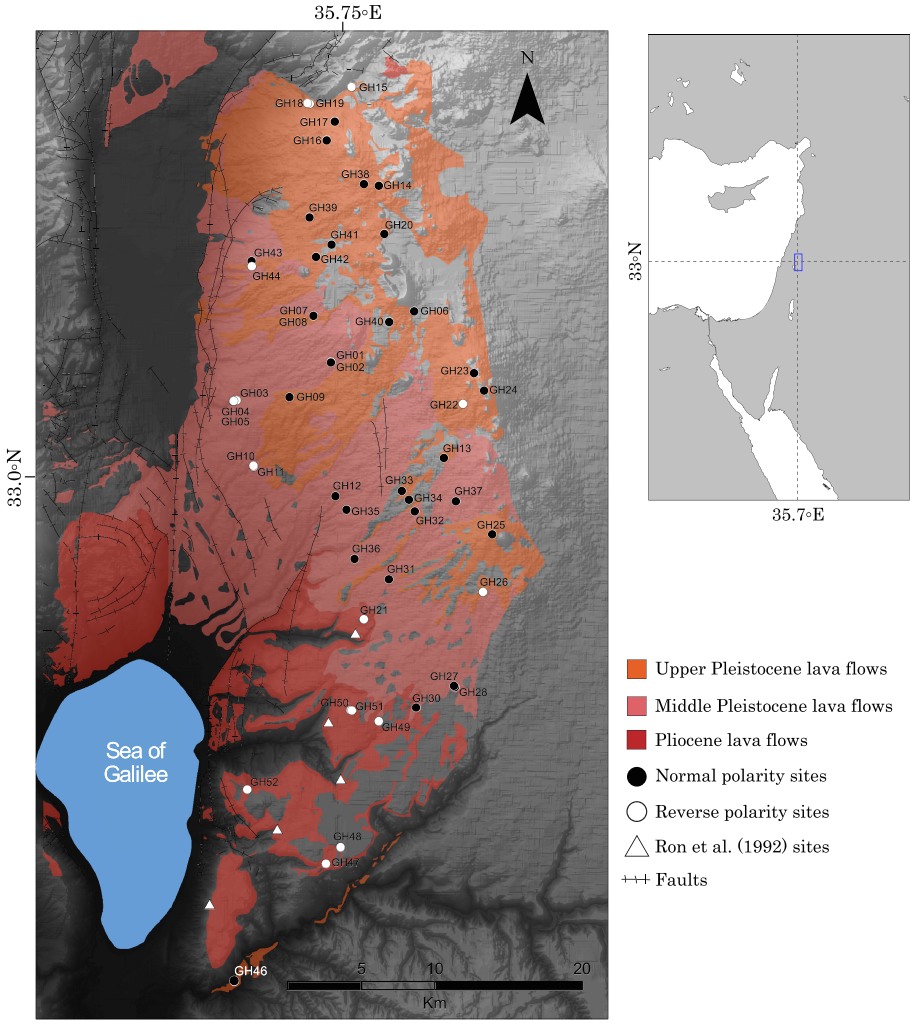

Figure 2. Location map. (left) Simplified geological map of the Golan Heights volcanic units on a digital elevation model map. The location area is shown as a frame in the right map. Paleomagnetic sites sampled from lava flows in this study are shown as black (normal polarity) or white (reverse polarity) filled circles. Triangles show locations of sites studied in the 1990s (Ron et al., 1992).

The ages of the exposed volcanic units generally decrease northeastward, where the Pliocene units, exposed in southern GH, are overlain by the Pleistocene units in central and northern GH (Figure 2). The ages of the Pliocene units range from 5.5 to 3.4 Ma based on 13 $^{40}Ar/^{39}Ar$ ages (Heimann et al., 1996; Table S1, supporting information). The ages of the Pleistocene volcanic units range from 1 to 0.1 Ma, based on 26 $^{40}Ar/^{39}Ar$ ages (Feraud et al., 1983; Inbar & Gilichinsky, 2009; Shaanan et al., 2010; Weinstein et al., 2013; Table S1, supporting information). The majority of the Pleistocene $^{40}Ar/^{39}Ar$ ages are from northeastern GH, thus, the exact age range of the Pleistocene units is not well constrained.

The GH is located east of the Dead Sea Transform (DST) plate boundary that separates the Arabian plate and Sinai microplate (Figure 2). Unlike the Galilee in the western side of the DST, which experienced extensive faulting and block rotations (Ron et al., 1984), it is presumed that the GH did not undergo significant deformation since the Pliocene. While the GH margins are quite faulted, only a few faults have been detected on the GH plateau (Figure 2) and it is generally thought that the GH horizontal lava flows were not tilted or rotated since their formation (Heimann & Ron, 1993; Hurwitz et al., 2000; Ron et al., 1984). Hence, the GH plateau should be suitable for PSV studies.

In a previous paleomagnetic work published only as an internal report, Ron et al. (1992) attempted to constrain the tectonic movement of the Arabian plate using paleomagnetism. They conducted a paleomagnetic

study based on 46 Pliocene lava flows (sites). Forty one sites were sampled from five sequences of lava flows exposed in five canyons at the margins of the plateau (triangles in Figure 2) and six sites from a different location on the plateau. The study resulted in a paleomagnetic pole with a large uncertainty cone (A_{95}) that significantly deviates from the geographic pole.

3. Methods

3.1. $^{40}Ar/^{39}Ar$

Eighteen Pleistocene age sites, mainly from Central GH were selected for $^{40}Ar/^{39}Ar$ dating (Figure S1 in the supporting information). The locations were chosen in an attempt to improve the spatial and temporal distribution of the dated flows in the GH area. Groundmass basalt samples were dated using $^{40}Ar/^{39}Ar$ following the procedures outlined in Koppers et al. (2000, 2008), Koppers, Gowen, et al., (2011),Koppers, Russell, et al., (2011), Koppers (2003), and Koppers and Staudigel (2005). The samples were crushed to 200- to 300-μm grain sizes followed by an acid-leaching procedure to remove interfering signals from alteration minerals, if present. Groundmass materials were further separated by conventional magnetic separation techniques and hand picking under a binocular microscope to remove any remnants of alteration and/or phenocrysts. Between 10 and 50 mg of material were prepared for age dating. The incremental heating experiments were carried out on an ARGUS VI multicollector mass spectrometer in the OSU Argon Geochronology Laboratory. These experiments were carried out using a custom-build CO_2 laser and extraction line and typically include 40 incremental heating steps.

3.2. The 1990s Data Set (Pliocene)

We recovered the original measurement data from 40 sites out of 46 from the original 1990s data set. The remaining six missing sites are from one location ("Tel Abu Al-Eitar") in southeastern GH. Specimens from the 1990s data set were demagnetized only using alternating field (AF) method. From each site two specimens were demagnetized in 10 mT steps from 10 to 90 mT and additional four or five specimens were demagnetized in 20 mT steps from 20 to 80 mT. The measurement data were translated to MagIC format (Tauxe et al., 2016) and were reanalyzed together with the new data set discussed below.

3.3. The New Data Set (Plio-Pleistocene)

For this study, a total of 51 new paleomagnetic sites were sampled in the Golan Heights plateau (Figure 2; Table S2 in the supporting information). Forty-four sites were sampled from different units of Pleistocene age and seven sites were sampled from different units of Pliocene age. Only fresh, well preserved, lava flows located far from faults were sampled. From each site, 8–10 oriented cores (samples) 1″ in diameter were drilled using a gasoline-powered portable drill equipped with a water-cooled diamond bit. The cores were oriented with a Pomeroy orienting device using both magnetic and sun compasses. Each sample was cut in the laboratory into one or two specimens, 2.2 cm in length each. A minimum of eight specimens from each site were demagnetized: at least six specimens were subjected to stepwise AF demagnetization in 5- or 10-mT steps up to 110 or 120 mT, and at least two specimens from each site were subjected to stepwise thermal demagnetization in 50 °C steps until a complete demagnetization of the natural remanent magnetization (NRM). Moment measurements and AF demagnetizations were carried out using an automated 2G-SRM-750 superconducting rock magnetometer equipped with in-line two-axis AF coils. Thermal demagnetizations were done using a modified ASC-TD48 paleomagnetic oven. The experiments were performed in the magnetic shielded room in the paleomagnetic laboratory, named after the late Prof. H. Ron, in the Institute of Earth Sciences at the Hebrew University in Jerusalem.

3.4. Rock Magnetism

Thermomagnetic curves of low-field magnetic susceptibility (χ) were measured on crushed samples from 40 sites using an AGICO MFK1-FA Kappabridge, equipped with a CS4 furnace under argon atmosphere. Measurements were made from room temperature to 700 °C.

Polished core samples were prepared from six samples representing different behaviors in the thermomagnetic curves. The polished samples were analyzed with electron microscopy using an FEI Quanta 200 Environmental Scanning Electron Microscope (ESEM) in a backscattered (BSE) mode. The SEM analysis was carried out in the Center for Nanoscience and Nanotechnology at the Hebrew University in Jerusalem.

3.5. Data Analysis

Data analysis was done using the Demag-GUI program, which is part of the PmagPy software package (Tauxe et al., 2016, https://earthref.org/PmagPy/). The demagnetization data were plotted on Zijderveld diagrams (Zijderveld, 1967) and the characteristic remanent magnetization (ChRM) vectors were calculated using principal component analysis (PCA; Kirschvink, 1980), where only vectors with MAD (Kirschvink, 1980) < 5 and DANG (Tauxe & Staudigel, 2004) < 5 were accepted. Site means were calculated using Fisher statistics (Fisher, 1953). All measurement data were translated to the MagIC format (Tauxe et al., 2016) and were uploaded to the MagIC database with their corresponding interpretations (https://www2.earthref.org/MagIC).

4. Results

4.1. $^{40}Ar/^{39}Ar$

Table 1 lists the $^{40}Ar/^{39}Ar$ plateau ages of 18 lava flows dated in this study (detailed results are given in Table S3 in the supporting information). Fourteen samples show age uncertainties less than 2% (between 1.6 and 5.6 ka, 2σ) and four samples show age uncertainties less than 3.5% (between 5.9 and 13.4 ka, 2σ). Except for two miniplateaus (34–44%) all samples have wide age plateaus (54–100%) and good MSWD statistics ranging from 0.61 to 1.79, with one sample higher at 2.22. The histograms in Figure 3 show distributions of all the 57 $^{40}Ar/^{39}Ar$ ages in the study area. The 39 ages dated in previous studies are shown in orange, and the 18 new ages from this study are shown in blue. Figure 3a shows that the new ages improve the Pleistocene geochronology, indicating nearly continuous activity during the past 1.1 Ma. In addition, the new data reveal previously unknown volcanic episodes near 1.5 and 2.6 Ma.

4.2. Demagnetization Data and Rock Magnetism

Our new data set consists of 436 specimens from 51 lava flows (sites). The majority of the specimens (80%) yield straight Zijderveld plots converging to the origin (Figure 4a), with MAD and DANG values less than 2°. In some cases, a secondary component is removed after 10–20 mT or 150–250 °C. The samples can be classified roughly into two groups: group A—left panel in Figure 4, and group B—right panel in Figure 4. The classification is based on the behavior during the demagnetization experiments, the thermomagnetic curves and mineralogical textures in the backscattered images. Group A exhibits high unblocking temperatures (T_{UB}) with median destructive temperature (MDT) above 350 °C, high coercivities with median destructive field (MDF) higher than 30 mT (Figure 4b), a sharp susceptibility drop at temperatures above 550 °C (labeled "high Tc" in Figure 4c), and Fe-oxides crystals with exsolution patterns of magnetite-ilmenite lamellae (sample GH22E in Figure 3d; Figure S2a in the supporting information). Group B exhibits low T_{UB} with MDT below 300 °C, low coercivities with MDF below 30 mT (Figure 4b), susceptibility drop at low and/or moderate temperatures (labeled "low/moderate Tc" in Figure 4c), and unexsolved titanomagnetites with varying titanium content and various sizes and morphologies (sample GH12E in Figure 3d; Figure S2b in the supporting information). Out of the 40 thermomagnetic curves, four samples do not fall into either of the above categories. We could not find any correlation between the magnetomineralogical group and other categories such as age, location, quality of the demagnetization data (expressed as MAD and DANG values), and quality of the paleomagnetic site mean (expressed as Fisher's k or α_{95} statistics). We therefore conclude that both groups are equivalently suitable for paleomagnetic and paleosecular variation analysis.

4.3. Paleomagnetic Poles

4.3.1. The 1990s Data Set (Pliocene)

The 1990s data set consists of 40 reverse polarity paleomagnetic site mean directions (Table 2). The site means were transformed into virtual geomagnetic poles (VGPs) and are plotted on a polar stereographic map in Figure 5a. The VGPs are plotted using five different colors representing the canyons from which they were sampled (Figure 5b). In each canyon the lowermost and uppermost lava flows from the sequence were dated (Figure 5c), yielding an age range of ~1.67 My, from 5.53 Ma to 3.86 Ma, presumably sufficient to average out secular variation effects. Yet, according to the geomagnetic polarity timescale (Gee & Kent, 2007) the geomagnetic field is in a reverse polarity state over less than half of this time interval. As we would expect to obtain both reverse and normal polarity states in this data set, these reverse polarity flows might actually represent a much shorter time interval than 1.67 My. In addition, it raises the possibility that identical

Table 1
$^{40}Ar/^{39}Ar$ Ages Dated in This Study

Site	Latitude	Longitude	Age type	Age (ka)	±2σ (ka)	^{39}Ar%	K/Ca	±2σ
GH01	33.06780	35.74018	Plateau	679.8	5.9	68	0.395	0.083
GH03	33.04463	35.67154	Plateau	1,111.5	5.3	53	0.652	0.036
GH05	33.04417	35.66922	Plateau	1,119.6	5.2	62	0.478	0.014
GH08	33.09605	35.72762	Plateau	103.9	1.8	98	0.215	0.072
GH09	33.04640	35.70973	Plateau	104.4	1.8	97	0.105	0.047
GH11	33.00444	35.68352	Plateau	1,584.8	9.0	54	0.341	0.055
GH12	32.98555	35.74288	Plateau	709.4	4.3	88	0.471	0.072
GH15	33.23632	35.75634	Plateau	841.5	5.6	73	0.493	0.071
GH17	33.20363	35.73782	Plateau	105.3	2.7	100	0.035	0.017
GH18	33.22599	35.72582	Plateau	891.2	13.4	76	0.401	0.066
GH22	33.04162	35.83600	Plateau	1,413.2	4.6	44	0.831	0.128
GH24	33.04974	35.85139	Plateau	615.5	3.0	66	0.528	0.082
GH25	32.96154	35.85678	Plateau	111.5	3.6	83	0.366	0.107
GH27	32.86815	35.82887	Mini Plateau	2,651.8	6.8	34	0.591	0.073
GH32	32.97603	35.80064	Plateau	556.6	3.0	72	0.419	0.081
GH33	32.98856	35.79130	Plateau	108.9	1.6	90	0.676	0.115
GH39	33.15644	35.72501	Plateau	120.6	3.2	91	0.245	0.054
GH43	33.12978	35.68269	Plateau	108.8	2.6	88	0.036	0.016

geomagnetic field states might have been oversampled. Figure 5a shows that the majority of the VGPs are clustered in groups according to the canyon from which they were sampled. The VGPs from Nahal El-Al, Afiq, and Mevo Hama, have the same age range within the C3n.2r reverse chron (4.62–4.8 Ma) but are clustered in three different groups, which are nearly 40° apart. The same is true for Nahal Daliot and Nahal Sameq, which are of the same nominal age but with different VGP locations. The grouping of the VGPs according to the sampling localities can be explained in two ways: One option is that the five canyons, which are located only few kilometers from the DST faults (Meiler, 2011; Figure 5b) are affected by tectonic block rotations. Another explanation is that each sequence of lava flows represents a time interval which is too short to fully accumulate PSV. While there is no way of discriminating between these two options for explaining the VGP distribution, we think that the tectonic mechnism is more likely. Regardless the explanation, as we cannot be confident that these blocks were not tilted, we choose to exclude the 1990s data set from further paleosecular variations analysis.

4.3.2. The New Data Set (Plio-Pleistocene)

The new data set consists of 51 paleomagnetic site mean directions (Table 3). Figure 6 shows the paleomagnetic site mean directions plotted on equal area projections using three different sets of selection criteria

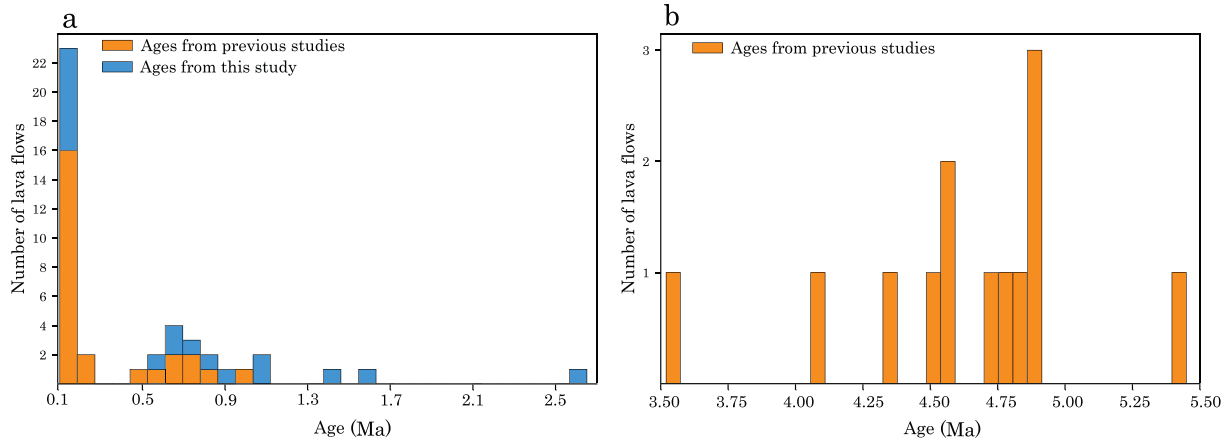

Figure 3. Distribution of the $^{40}Ar/^{39}Ar$ ages of lava flows and scoria cones in the Golan Heights plateau. Orange (blue) bars are ages dated in previous studies (this study). a) Pleistocene ages, b) Pliocene ages.

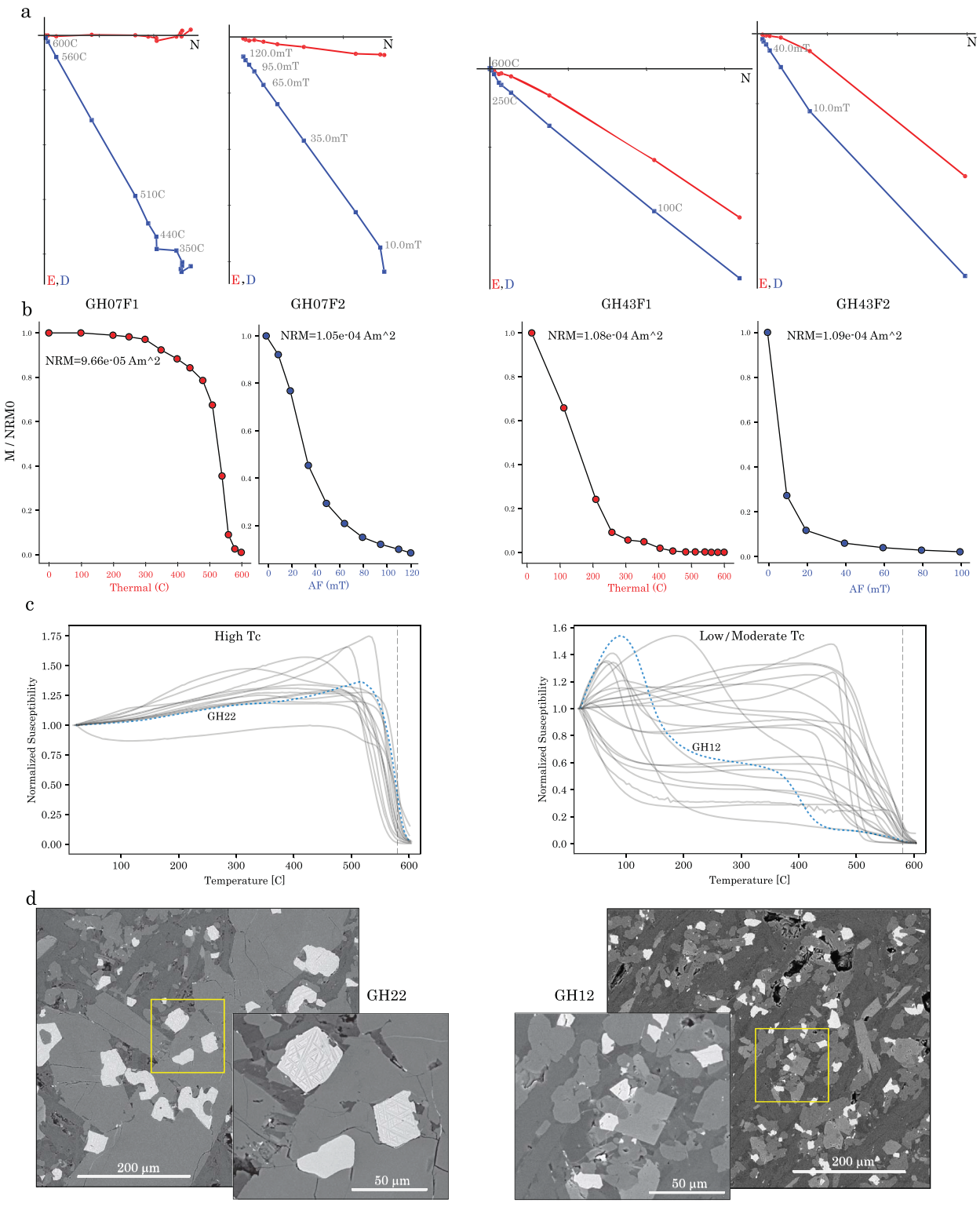

Figure 4. Representative demagnetization results and rock magnetic data. (a) Zijderveld diagrams of thermal and alternating field demagnetization done on sister specimens from the same mother samples. (b) Demagnetization curves of the same specimens in (a) showing two behaviors: high coercivity and high T_{UB} (left) and low coercivity and low T_{UB} (right); (c) Thermomagnetic susceptibility curves (χ-T) grouped according to the temperature range of the main susceptibility drop: High T_C (left) and moderate/low T_C (right). Blue dashed curves are samples GH12 and GH22 shown in (d); (d) Representative Scanning Electron Microscope backscattered images of two different ferromagnetic phases: exsolved crystals consisting of ilmenite-magnetite lamellae (GH22E, left), nonexsolved titanomagnetite crystals (GH12E, right).

Table 2
Pliocene Paleomagnetic Site-Mean Directions From the 1990s Data Set

Site	Inc	Dec	α_{95}	k	n/N	VGP lat	VGP lon	Latitude	Longitude	Age (Ma)
af1	−54.2	160.0	3.5	489	5/6	−73.3	137.9	32.78340	35.69914	4.88 ± 0.10
af2	−56.6	156.8	5.7	1948	2/6	−70.5	145.2	32.78340	35.69914	4.98–4.37
af3	−55.4	151.5	5.9	1782	2/6	−66.3	141.3	32.78340	35.69914	4.98–4.37
af4	−52.2	153.0	5.0	2485	2/6	−67.4	133.2	32.78340	35.69914	4.98–4.37
af5	−55.5	149.8	4.6	2976	2/6	−65.0	141.6	32.78340	35.69914	4.59 ± 0.22
mh1	−29.7	206.0	17.3	210	2/6	−61.1	335.0	32.73579	35.65193	4.88 ± 0.07
mh2	−35.5	200.1	2.8	578	6/6	−67.8	336.8	32.73579	35.65193	4.95–4.12
mh3	−32.4	205.4	1.8	1450	6/6	−62.6	333.0	32.73579	35.65193	4.95–4.12
mh4	−31.3	197.1	14.0	319	2/6	−67.9	347.3	32.73579	35.65193	4.95–4.12
mh5	−34.0	196.4	7.3	1174	2/6	−69.6	345.4	32.73579	35.65193	4.95–4.12
mh6	−31.4	205.3	6.6	105	6/6	−62.3	334.2	32.73579	35.65193	4.50 ± 0.38
nd1	−28.8	196.9	10.8	51	5/6	−66.7	350.6	32.89943	35.76627	4.43 ± 0.10
nd10	−36.5	183.7	7.2	293	3/6	−77.0	20.2	32.89943	35.76627	4.53–3.86
nd11	−37.7	176.2	6.5	199	4/6	−77.8	52.7	32.89943	35.76627	4.53–3.86
nd12	−36.4	176.6	4.2	340	5/5	−77.0	50.1	32.89943	35.76627	4.53–3.86
nd13	−41.2	178.6	29.8	8	5/6	−80.7	43.7	32.89943	35.76627	4.53–3.86
nd14	−34.7	178.8	3.9	298	6/6	−76.2	40.5	32.89943	35.76627	4.53–3.86
nd15	−37.0	186.2	3.4	514	5/6	−76.6	10.0	32.89943	35.76627	4.53–3.86
nd16	−34.4	176.0	4.7	268	5/6	−75.5	51.1	32.89943	35.76627	3.97 ± 0.11
nd2	−40.1	202.5	3.9	289	6/6	−67.8	326.9	32.89943	35.76627	4.53–3.86
nd3	−35.8	200.1	6.2	153	5/6	−67.8	336.9	32.89943	35.76627	4.53–3.86
nd4	−27.3	184.7	6.1	230	4/6	−71.1	21.6	32.89943	35.76627	4.53–3.86
nd5	−27.2	194.7	11.4	485	2/6	−67.2	356.4	32.89943	35.76627	4.53–3.86
nd6	−35.8	191.5	3.2	356	7/7	−73.4	354.8	32.89943	35.76627	4.53–3.86
nd7	−36.0	184.4	3.3	420	6/6	−76.5	17.8	32.89943	35.76627	4.53–3.86
nd8	−40.3	181.2	6.7	130	5/6	−80.0	29.4	32.89943	35.76627	4.53–3.86
nd9	−35.4	184.4	5.9	169	5/7	−76.1	18.3	32.89943	35.76627	4.53–3.86
ne1	−31.5	168.9	8.1	944	2/5	−71.3	70.8	32.80937	35.74199	4.82 ± 0.37
ne2	−30.5	164.1	3.1	616	5/6	−68.2	80.8	32.80937	35.74199	5.19–4.40
ne3	−32.9	160.3	1.9	4004	3/6	−66.9	90.5	32.80937	35.74199	5.19–4.40
ne4	−31.1	163.2	7.0	120	5/6	−67.9	83.2	32.80937	35.74199	5.19–4.40
ne5	−57.6	168.4	3.3	413	6/6	−79.1	158.9	32.80937	35.74199	5.19–4.40
ne6	−56.4	175.1	2.7	628	6/6	−84.2	173.1	32.80937	35.74199	5.19–4.40
ne7	−55.1	190.6	2.2	771	7/7	−80.8	285.0	32.80937	35.74199	4.55 ± 0.15
ns1	−53.1	169.3	2.8	587	6/6	−81.0	133.9	32.84816	35.73688	5.45 ± 0.08
ns2	−53.6	178.3	8.9	790	2/6	−88.1	168.6	32.84816	35.73688	5.53–3.90
ns3	−33.9	162.4	2.0	1136	6/6	−68.7	87.9	32.84816	35.73688	5.53–3.90
ns4	−27.3	165.7	2.9	519	6/6	−67.5	74.4	32.84816	35.73688	5.53–3.90
ns5	−23.6	166.8	4.7	206	6/6	−66.2	69.3	32.84816	35.73688	5.53–3.90
ns6	−30.4	164.0	16.5	230	2/5	−68.1	80.8	32.84816	35.73688	4.06 ± 0.16

Note. Inc, Dec: site's mean inclination and declination, respectively; α_{95}: 95% confidence cone about the mean; *k*: precision parameter (Fisher, 1953); n/N: number of specimens used to calculate the mean out of the total; VGP lat/lon: virtual geomagnetic pole's latitude and longitude, respectively; Latitude, Longitude: Paleomagnetic site coordinates; Age: with ± indicates $^{40}Ar/^{39}Ar$ age, age range represents an estimate based on field relations.

defined by cutoff values for n (number of specimens per site) and k (Fisher precision parameter, Fisher, 1953). We did not include a criterion for excluding "excursional" data with VGP located far from the geographic pole. The first subset (Figure 6a), with no selection criteria applied, consist of 33 normal polarity sites and 18 reverse polarity sites, with two anomalous "excursional" data with low inclination and large declinations. The second subset (Figure 6b) uses the criteria used by Cromwell et al. (2018) for the PSV10 compilation ($n \geq 4$ and $k \geq 50$). Forty-five sites pass these criteria with 28 normal polarity and 17 reverse polarity sites. Here, the two anomalous "excursional" sites (sites GH09, GH51) fail these criteria. The third subset (Figure 6c) uses the criteria suggested by Tauxe et al. (2003) with $n \geq 5$ and $k \geq 100$. Forty-four sites pass these criteria with 27 normal polarity and 17 reverse polarity sites. Only one site in the second subset is rejected in the third data set. The right panel in Figure 6 shows bootstrap reversal test (Tauxe et al., 1991) displayed as cumulative distributions of the Cartesian components of the bootstrap means with their 95% level of confidence (instead of as histograms in the original paper). In all three data sets the normal

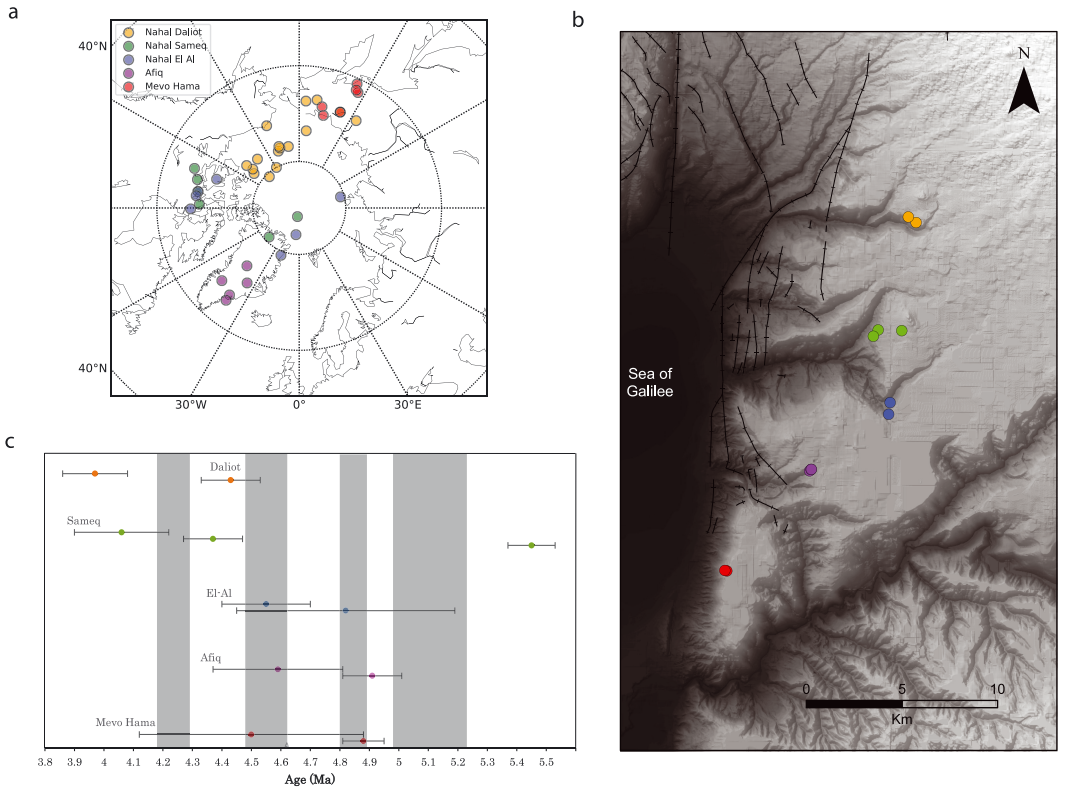

Figure 5. Pliocene paleomagnetic data following Ron et al. (1992). (a) Virtual geomagnetic poles plotted on a polar stereographic map. All directions are reversed polarity. Each color represents a canyon from which sites were sampled. (b) Southern Golan Heights digital elevation model map showing the location of the sampled canyons (same colors as in [a]). (c) Age ranges of the upper and the lower flow in each sequence, where all ages are $^{40}Ar/^{39}Ar$ (Heimann et al., 1996) except Nahal Daliot that was dated with K-Ar (Mor, 1993). Color scheme as in (a) and (b). Dark (white) intervals denote normal (reverse) subchrons.

directions (red) and the antipodal of the reverse directions are statistically indistinguishable, thus passing the reversals test.

For each one of the three sets shown in Figure 6 the site mean directions were transformed into VGPs and the paleomagnetic poles were calculated by averaging the VGPs (Table 4). The VGPs and the paleomagnetic poles are plotted on polar stereographic maps in Figures 7a–7c. An inclination anomaly (ΔI) for each set was calculated by (1) calculating from the averaged pole the direction at a common reference location (33°N, 35.75°E) representing the GH, then (2) subtracting the resulting inclination from GAD inclination at 33°N. For the three sets of selection criteria, the A_{95} confidence cones includes the geographic pole and the inclination anomaly calculated from the averaged pole is nearly zero (Table 4).

Figures 7d–7f show an alternative calculation of the paleomagnetic pole and the inclination anomaly using a statistical bootstrap (Tauxe et al., 1991). For this we used 10,000 synthetic paleomagnetic poles calculated from pseudo-sample sets consisting of N VGPs drawn randomly with replacement, where N is the number of VGPs in the original sample set being tested. The resulting bootstrapped mean VGP, the median ΔI, and the 95% confidence interval of the ΔI values are listed in Table 4, showing similar results to the Fisher means. The 95% bootstrap confidence bounds for the inclination anomaly include zero. From the bootstrap poles we also calculate the declination anomaly. The median and the 95% confidence bounds of the declination anomaly are biased toward positive declinations, but zero declination anomaly is included in the 95% confidence interval. Thus, also in the bootstrap analysis the geographic pole is included in the 95% confidence interval, in agreement with a GAD structure. It can be seen that the distribution of synthetic VGP means is elongated, with a long axis nearly perpendicular to the GH longitude line. This might be an effect of minor small-scale tectonic rotations about a vertical axis. This elongation does not affect the inclination.

Table 3
Plio-Pleistocene Paleomagnetic Site-Mean Directions From this Study

Site	Inc	Dec	α_{95}	k	*n*/*N*	VGP lat	VGP lon	Latitude	Longitude	Age (ka)
GH01	37.2	350.0	4.7	168	7/15	74.8	254.1	33.06780	35.74018	679.8 ± 5.9
GH02	37.2	349.7	2.3	575	8/8	74.7	255.0	33.06746	35.74018	1200–700
GH03	−56.9	157.0	2.3	498	9/9	−70.8	145.5	33.04463	35.67154	1111.5 ± 5.3
GH04	−58.0	175.1	2.1	543	10/10	−83.1	181.8	33.04396	35.66901	1600–700
GH05	−56.8	181.0	2.8	307	10/15	−85.6	226.0	33.04417	35.66922	1119.6 ± 5.2
GH06	50.0	5.7	2.3	521	9/9	84.6	149.8	33.09859	35.80091	500–100
GH07	55.8	5.3	3.1	283	9/11	85.1	95.4	33.95970	35.72762	1200–700
GH08	59.0	11.6	2.4	540	8/8	78.5	86.8	33.09605	35.72762	103.9 ± 1.8
GH09	27.8	84.9	9.9	47	6/7	12.2	115.9	33.04640	35.70973	104.4 ± 1.8
GH10	−56.8	175.7	2.4	522	8/8	−84.4	178.2	33.00390	35.68372	1600–700
GH11	−49.3	214.4	2.5	505	8/8	−60.7	301.9	33.04440	35.68352	1584.8 ± 9.0
GH12	44.9	2.2	4.6	176	7/8	83.2	198.8	32.98555	35.74288	709.4 ± 4.3
GH13	59.8	25.3	6.1	83	8/9	68.4	97.8	33.00856	35.82204	500–100
GH14	49.7	348.8	13.4	14	10/10	80.1	293.2	33.17375	35.77575	500–100
GH15	−43.3	196.1	3.2	348	7/7	−73.9	331.3	33.23632	35.75634	841.5 ± 5.6
GH16	57.8	2.7	3.1	470	6/8	84.3	57.7	33.21511	35.74377	500–100
GH17	47.2	9.5	3.5	247	8/8	80.5	153.9	33.20363	35.73782	105.3 ± 2.7
GH18	−47.8	183.8	4.1	185	8/8	−84.6	357.9	33.22599	35.72582	891.2 ± 13.4
GH19	−52.2	180.9	2.3	883	6/7	−89.1	334.6	33.22658	35.72400	1600–700
GH20	52.7	1.0	3.5	301	7/8	89.2	116.5	33.14600	35.77943	500–100
GH21	−39.0	178.7	2.7	507	7/7	−79.1	42.1	32.91003	35.76308	4800–4600
GH22	−55.7	165.5	3.8	219	8/8	−77.7	144.9	33.04162	35.83600	1413.2 ± 4.6
GH23	51.6	30.8	3.6	275	7/7	64.1	119.1	33.06038	35.84427	500–100
GH24	43.0	31.8	4.7	140	8/9	61.2	133.7	33.04974	35.85139	615.5 ± 3.0
GH25	64.9	338.0	16.6	12	8/8	68.3	352.1	32.96154	35.85678	111.5 ± 3.6
GH26	−59.9	214.0	4.8	104	10/11	−61.9	279.8	32.92633	35.84982	2500–780
GH27	46.9	356.3	4.9	127	8/8	84.3	250.6	32.86815	35.82887	2651.8 ± 6.8
GH28	44.1	3.3	3.1	459	6/7	82.4	192.7	32.86889	35.82825	2600–780
GH30	50.8	4.1	2.9	359	8/8	86.3	145.9	32.85580	35.80069	1600–700
GH31	43.0	352.6	3.1	319	8/8	79.8	256.8	32.93434	35.78133	1600–700
GH32	52.2	336.6	17.2	10	9/10	70.4	311.7	32.97603	35.80064	556.6 ± 3.0
GH33	59.9	7.4	4.7	120	9/10	80.2	70.8	32.98856	35.79130	108.9 ± 1.6
GH34	59.8	18.4	2.2	761	7/8	73.4	92.9	32.98312	35.79625	100–780
GH35	62.2	2.1	2.1	675	8/8	79.4	44.0	32.97711	35.75094	1600–700
GH36	28.4	326.7	15.8	19	6/9	55.0	283.2	32.94704	35.75662	1600–700
GH37	40.8	350.4	2.3	558	8/8	77.2	259.5	32.98198	35.83036	1600–700
GH38	47.2	9.1	2.1	721	8/8	81.3	149.3	32.17677	35.76476	500–100
GH39	59.6	17.3	2.9	445	7/8	74.4	93.0	33.15644	35.72501	120.6 ± 3.2
GH40	57.3	356.9	3.6	287	7/8	84.6	9.0	33.09204	35.78264	500–100
GH41	53.0	16.2	5.7	111	7/8	76.5	119.5	33.13965	35.74096	500–100
GH42	49.9	2.5	3.1	323	8/8	86.8	174.0	33.13217	35.72959	500–100
GH43	51.1	19.9	5.2	134	7/8	73.2	124.8	33.12978	35.68269	108.8 ± 2.6
GH44	−58.0	230.7	4.0	374	5/10	−49.1	283.0	33.12659	35.68304	1600–780
GH45	49.1	31.5	3.9	235	7/8	63.1	122.9	32.68955	35.66908	500–100
GH46	46.7	24.0	5.5	147	6/8	68.8	132.2	32.68919	35.66756	500–100
GH47	−53.1	151.5	2.5	577	7/8	−66.2	135.8	32.76036	35.73468	4950–4120
GH48	−65.1	144.3	2.7	359	9/9	−59.5	164.4	32.77044	35.74530	4950–4120
GH49	−57.6	175.0	3.8	257	7/8	−83.3	180.1	32.84762	35.77367	4950–4120
GH50	−29.8	165.1	2.8	389	8/8	−68.4	77.9	32.85442	35.75322	5530–3900
GH51	−7.8	133.0	180.0	3	3/8	−37.5	102.6	32.85407	35.75411	5530–3900
GH52	−34.2	160.6	3.4	268	8/8	−67.7	91.5	32.80608	35.67796	4980–4370

Note. Inc, Dec: site's mean inclination and declination, respectively; α_{95}: 95% confidence cone about the mean; *k*: precision parameter (Fisher, 1953); *n*/*N*: number of specimens used to calculate the mean out of the total; VGP lat/lon: virtual geomagnetic pole's latitude and longitude, respectively; Latitude, Longitude: Paleomagnetic site coordinates; Age with ± indicates $^{40}Ar/^{39}Ar$ age, age range represents an estimate based on field relations.

A VGP scatter parameter (S_B) was calculated for each of the subsets described above, following Biggin et al. (2008): $S_B = \sqrt{\frac{1}{N-1}\sum_{i=1}^{N}\left(\theta_i^2 - \frac{S_{W_i}^2}{n_i}\right)}$, where θ_i is the angle between the VGP_i and the geographic pole and

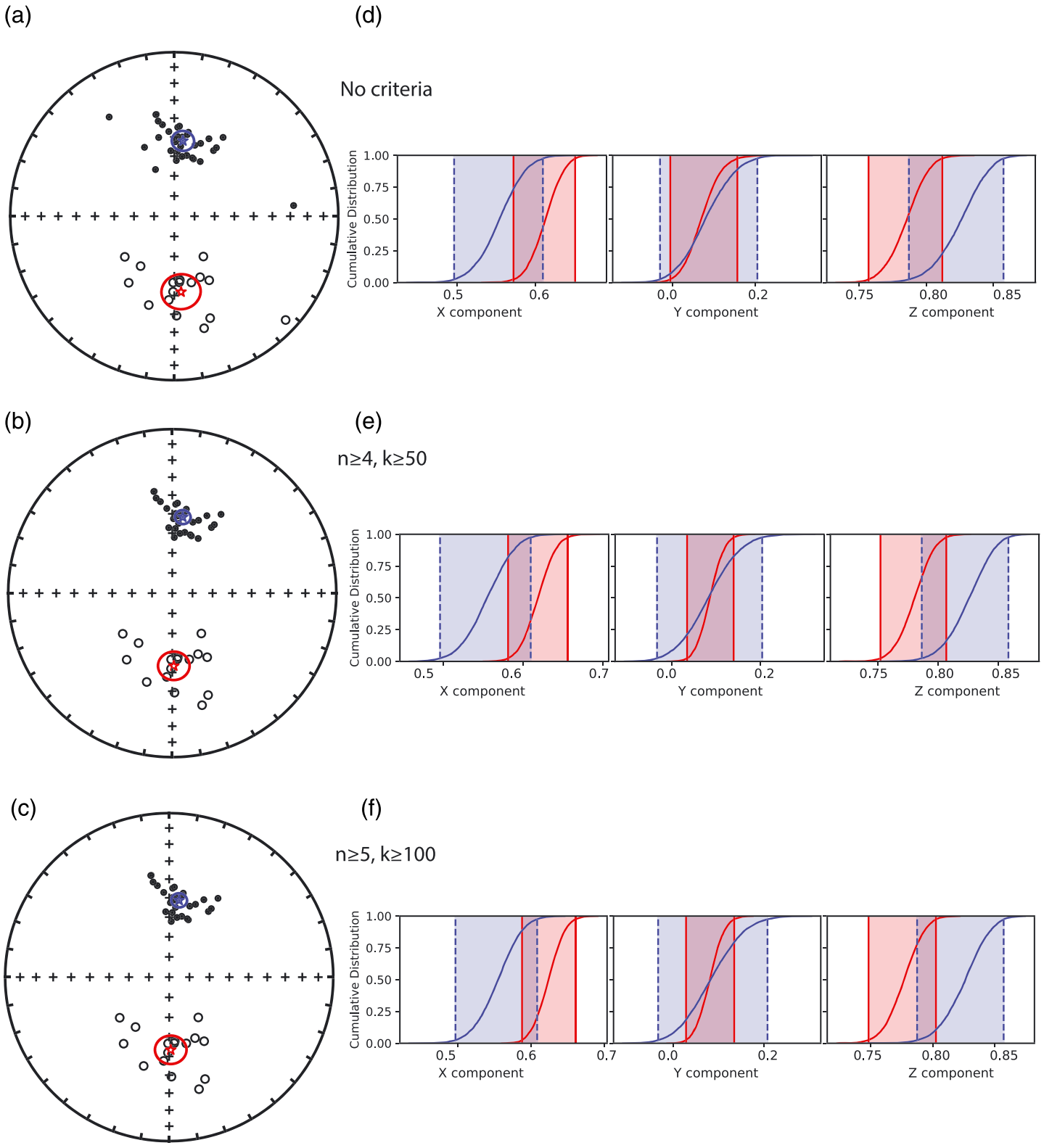

Figure 6. Paleomagnetic site mean directions. (a–c) Equal area projections of the site mean directions. (d–f) Reversal test displayed as cumulative distributions of Cartesian components of bootstrapped means from 1,000 pseudo-samples from data in (a)–(c), respectively, where red (blue) are normal (antipodal of the reversed) polarity directions. Each row displays different selection criteria: (a, d) No selection criteria; (b, e) $n \geq 4$, $k \geq 50$; (c, f) $n \geq 5$, $k \geq 100$.

Table 4
Paleomagnetic Poles and Inclination Anomalies

	Subset	Fisher mean[a]					Bootstrap[b]		
Selection criteria	N^c (N^d/R^e)	VGP (lat, lon)	k	A_{95}	ΔI	S_B (95% bounds)[f]	Mean VGP (lat, lon)	ΔI median, (95% bounds)	ΔD median, (95% bounds)
No selection criteria	51 (33/18)	87.6,117.0	15.0	5.3	0.4	21.0 (18.5, 24.3)	87.5, 116.9	0.3 (−2.2, 2.7)	2.86 (−3.2, 9.3)
$n \geq 4$, $k \geq 50$ (Cromwell et al., 2018)	45 (28/17)	85.9,118.2	25.0	4.3	0.5	16.7 (14.6, 19.5)	85.9, 118.1	0.5 (−2.0, 2.7)	4.9 (−0.1, 9.9)
$n \geq 5$, $k \geq 100$ (Tauxe et al., 2003)	44 (27/17)	86.3,120.8	25.1	4.4	0.3	16.6 (14.5, 19.4)	86.3, 121.0	0.2 (−2.3, 2.6)	(4.4, −0.5, 9.5)

Note. VGP = virtual geomatic pole.
[a]Pole and inclination anomaly calculated by Fisher mean of VGP. [b]Pole and inclination anomaly calculated using bootstrap analysis of VGPs (see text for details). [c]Number of sites in the subset. [d]Normal polarity sites. [e]Reverse polarity sites. [f]Calculated following Cox (1969, 1970).

$S_{W_i} = \frac{81}{\sqrt{K_i}}$ is the within-site scatter calculated using the k_i Fisher precision parameter in the pole space. K_i is calculated from the Fisher precision parameter in the direction space (k_i) using equation (12) in Cox (1970): $K = \frac{8k}{5+18\sin^2\lambda+9\sin^4\lambda}$,where λ is the site paleolatitude. The scatter parameters, listed in Table 4, are 21.0, 16.7, and 16.6 for the three sets, respectively. The reason for the difference in the scatter parameter for the first set (no acceptance criteria) is the addition of two sites (GH09, GH51) which have poor Fisher statistics and poles position near the equator. The values obtained after applying selection criteria are not far from the averaged value calculated from PSV10 compilation at latitude bin 30–40° (14.5) by Cromwell et al. (2018).

5. Discussion

5.1. Inclination Anomaly

When discussing the latitudinal dependency of the geomagnetic inclination anomaly, it is worth considering first the effect of the calculation method on the inclination anomaly values. Ideally, the averaged paleomagnetic vector would be a vector mean that takes into account both the direction and the intensity of each paleomagnetic vector. Yet in standard paleomagnetic analysis only site mean directions are calculated. Hence, the averaged paleomagnetic inclination is calculated from a mean of unit vectors, which leads to an inherent bias in the inclination anomaly (Creer, 1983). Figure 8 demonstrates this effect on two subsets of PSV10 compilation: PSV10-TB, and PSV10-TB_{vcut}. The former is the same as PSV10, but takes only the top and the bottom flows from consecutive or stacked lava flows, in order to remove oversampling bias (Cromwell et al., 2018). The latter excludes "excursional" VGPs from PSV10-TB for each latitud bin using the iterative method of Vandamme (1994; see also Cromwell et al., 2018). Figures 8a and 8d show the inclination anomaly in 10° latitude bins calculated following Cromwell et al. (2018). The inclination anomaly, plotted at the averaged latitude, is the Fisher mean of all the paleomagnetic directions in the bin. Figures 8b and 8e are the same as Figures 8a and 8d, but the directions are transformed to a common averaged latitude through a VGP transformation. This is done to account for the dependency of the inclination on latitude. In both calculation methods the bias due to unit vector averaging is evident, with a positive inclination anomaly in the Southern Hemisphere and a negative inclination anomaly in the Northern Hemisphere. This is also seen in the inclination anomaly calculated from TK03.GAD model. Although the model is based on an averaged GAD field structure (Tauxe & Kent, 2004) the inclination anomaly bias follows the same trend discussed above with negative (positive) anomalies in the Northern (Southern) Hemispheres. The magnitude of the bias depends on the characteristics of PSV. Thus, an inclination anomaly calculated this way can be thought as representing PSV. Figures 8b and 8e demonstrate that the absolute value of the inclination anomaly is suppressed when directions are transformed to a common latitude through VGP. It does not reduce, however, the hemispherical asymmetry shown in Figures 8a, 8d, and 1. In the northern hemisphere of Figures 8b and 8e, the absolute value of the inclination anomaly is less than 2° with error bars overlapping $\Delta I = 0$, with the exception of latitude bin 20–30°N that shows a relatively large negative anomaly around −5°. In the southern hemisphere of Figures 8b and 8e the inclination anomalies are larger but also more dispersed and have larger error bars.

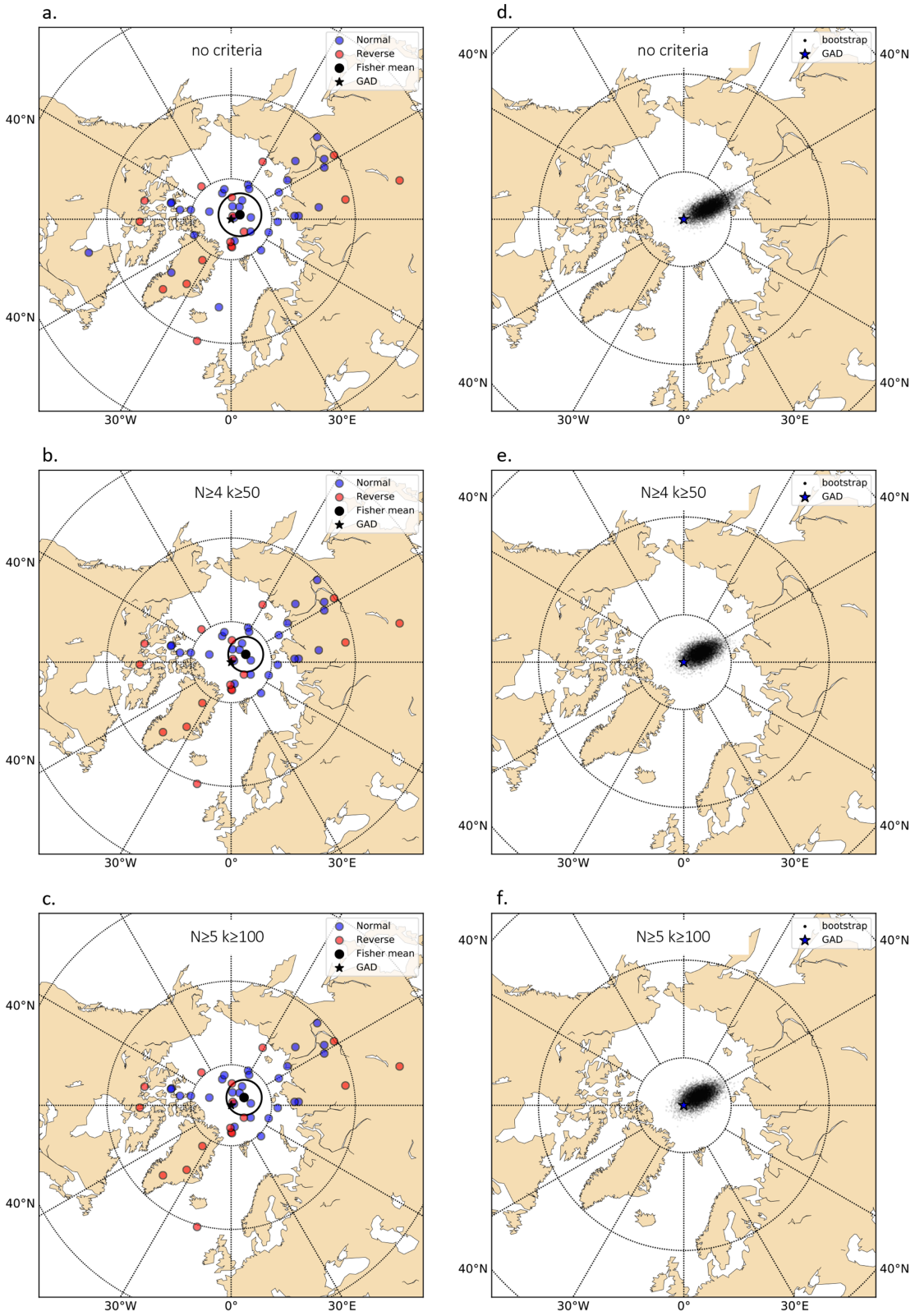

Figure 7. Virtual geomagnetic poles (VGP) and paleomagnetic poles. (a–c) VGPs and paleomagnetic pole calculated using Fisher statistics. (a) No selection criteria are applied; (b) selection criteria are $n \geq 4$, $k \geq 50$; (c) selection criteria are $n \geq 5$, $k \geq 100$. (d–f) Projection of 10,000 bootstrapped Fisher means of pseudo-samples drawn from the data in (a)–(c), respectively. GAD = geocentric axial dipole.

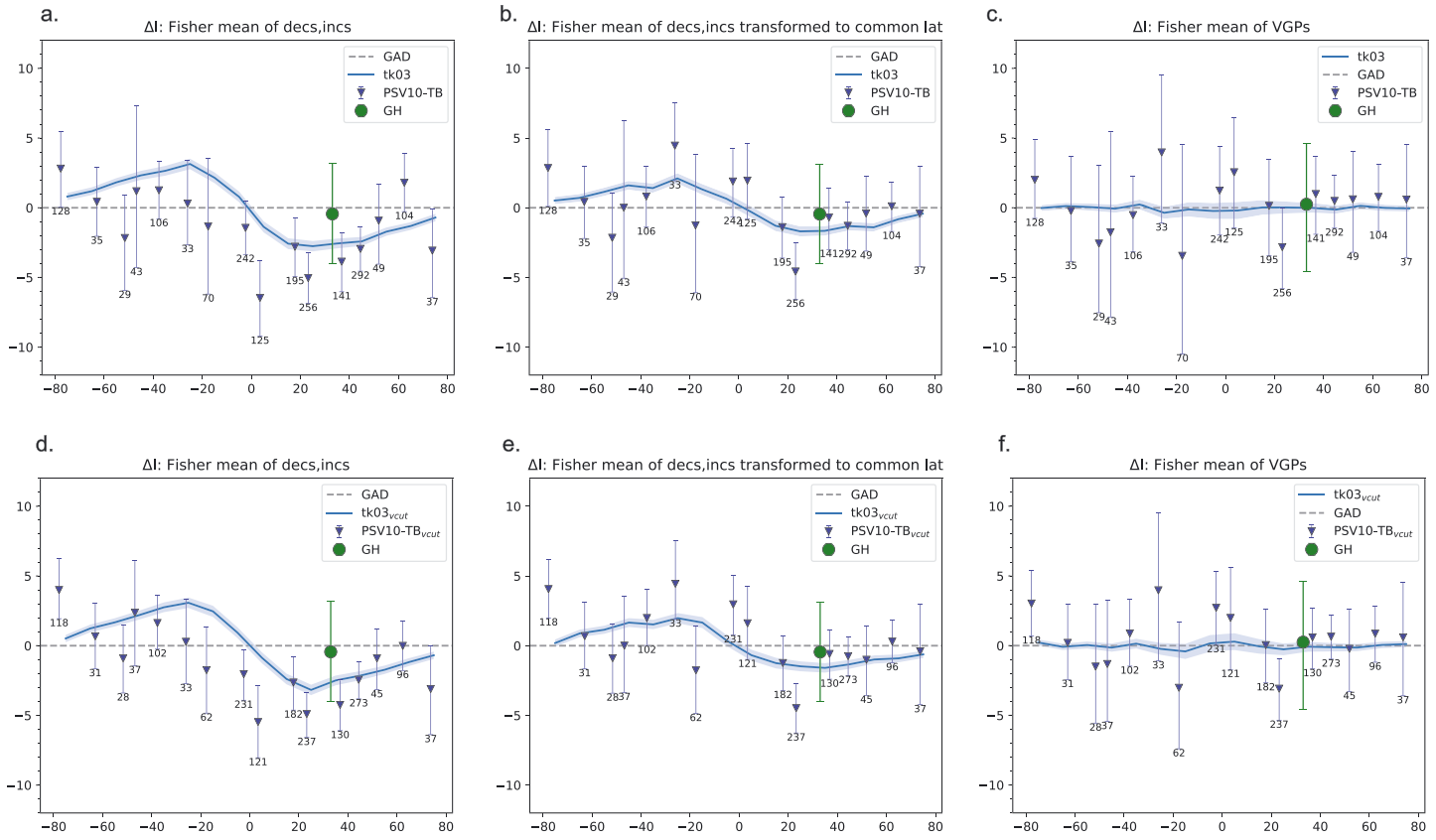

Figure 8. Averaged inclination anomaly (ΔI) per latitude bin using three methods to calculate the averaged paleomagnetic direction: (a, d) A mean of paleomagnetic directions within bin, (b, e) same as (a, d) but directions are corrected for common latitude using a VGP transformation, (c, f) directions are calculated from a mean of VGP. Solid line shows bootstrap means and 95% confidence intervals calculated from 10,000 directions for each bin drawn from TK03. GAD field model (Tauxe & Kent, 2004). Top (bottom) panels use the PSV10-TB (PSV10-TB$_{vcut}$) subset of the PSV10 compilation (see text for details). ΔI calculated from the Golan Heights data set is shown as green circle. VGP = virtual geomagnetic pole.

Figures 8c and 8f show an alternative way to calculate the inclination anomaly: by averaging VGPs instead of paleomagnetic directions. The inclination anomalies calculated this way are statistically indistinguishable from $\Delta I = 0$ with one exception at bin 20–30° (Figure 8f). These observations suggest that the underlying field model in PSV10 compilation is a GAD.

Figure 8 also shows the inclination anomaly calculated from GH (using the stricter selection criteria of Tauxe et al., 2003, Table 4) compared to the PSV10 compilation. When calculating the inclination anomaly as a mean of directions (Figures 8a and 8d), the GH inclination anomaly ($\Delta I = -0.4°$) is lower than the global data and the prediction of TK03. This is because the latitude difference between the sites in the GH data set is only a degree, therefore the bias due to latitudinal dependence of the inclination is negligible in GH. When directions are transformed to common latitude (Figures 8b and 8e) or calculated from a VGP mean (Figures 8c and 8f) the GH anomaly ($\Delta I = -0.5°$, 0.25° for Figures 8b, 8e, and 8c, 8f, respectively) is similar to the northern hemisphere data in latitude bins 10–80°N with the exception of the anomalous value at 20–30°N discussed above. Also, the GH values with their error bar are close to the TK03 model prediction.

Taken altogether, it seems that the GH data are in agreement with Northern Hemisphere data when using VGP transformation to calculate the inclination anomaly, either by averaging directions or by averaging VGPs. The new GH data set suggests that the anomalous averaged inclination anomaly in 20–30°N latitude bin might be an artifact value that requires further inspection or a result of a complex nonzonal contributions to the TAF.

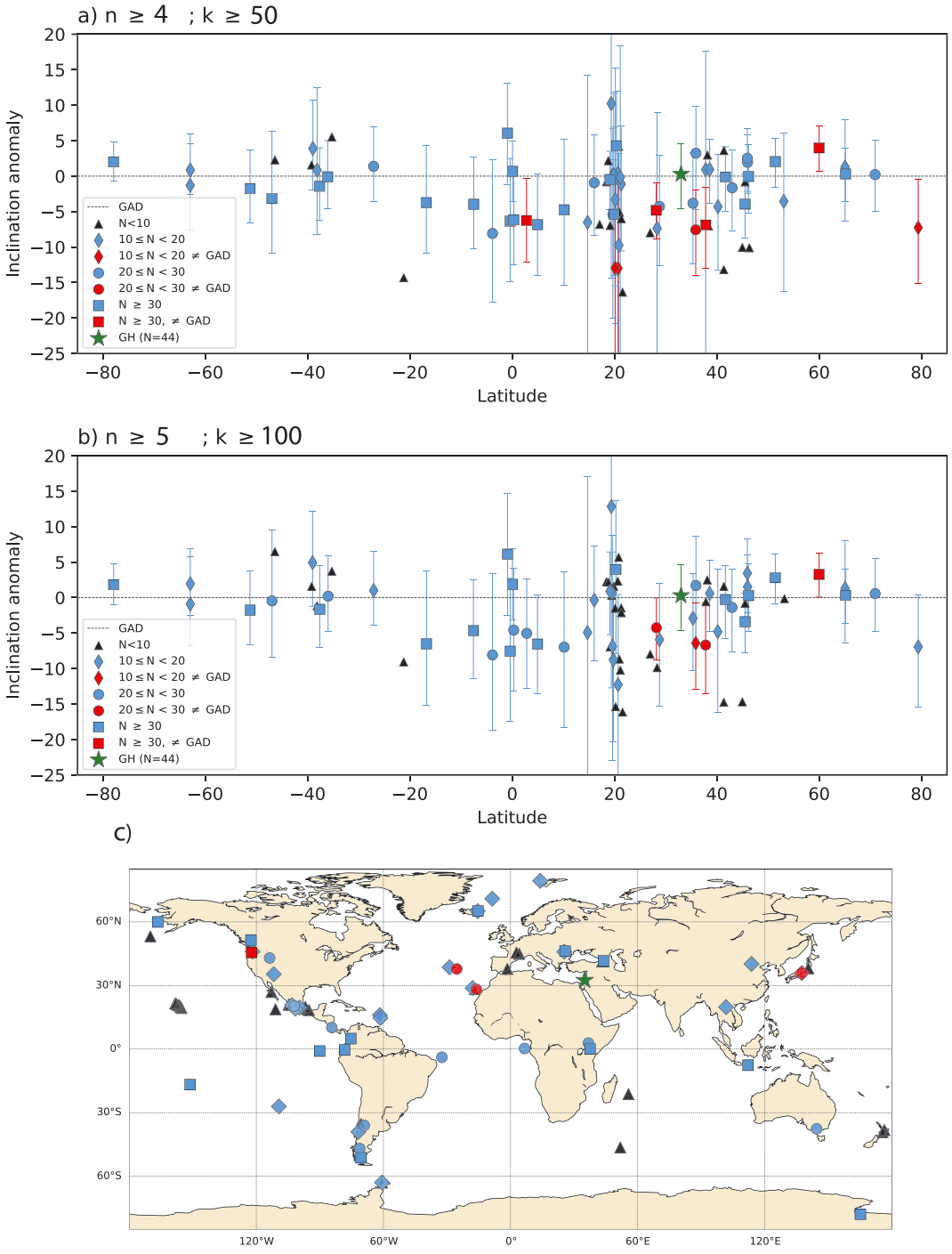

Figure 9. Inclination anomaly calculated from a mean of VGP per study in PSV10 compilation. Different symbols denote number of sites per study. Blue (red) color represents error bars, calculated from the A_{95} of the mean VGP, overlapping (not crossing) the horizontal line $\Delta I = 0$. (c) Location map of the data in (b). VGP = virtual geomagnetic pole.

5.2. The Effect of Selection Criteria and Data Reduction on the Inclination Anomaly

Figure 7 and Table 4 show that the GH data set is dominated by sites with $k > 100$ and $n \geq 5$ with 44 sites passing these criteria. As noted by Cromwell et al. (2018), most studied locations do not include so many sites with such high Fisher precision parameter. Thus, the global inclination anomaly in Cromwell et al. (2018) is calculated by stacking all sites with $k > 50$ and $n \geq 4$ within latitude bins. To inspect if the aberrant

inclination anomaly in 20–30°N (discussed in section 5.1) results from inclusion of poor-quality data in the calculation, we plot in Figure 9 the PSV10 compilation data as separate studies instead of as latitude bin means. We choose here to calculate the inclination anomaly from the mean VGP instead of mean of directions (i.e., similar to Figures 8c and 8f). We also exclude sites with VGP latitudes below 45° in order to include only "typical stable polarity" field estimates. We choose 45° as the cutoff for VGP latitude instead of using the Vandamme (1994) iterative method as sometimes locations do not include enough sites for the proper use of this method. Figures 9a and 9b show the inclination anomaly calculated from each study in PSV10 compilation with different selection criteria (i.e., cutoff values of n and k as in Figures 6 and 7). The different symbols denote the number of sites per study, and red symbols represent mean inclination anomalies that do not include the zero. It can be seen that most studies with number of sites (N) > 10 are in agreement with a GAD field model (blue symbols). Only a few studies show a nonzero inclination anomaly, but the number of such studies is reduced to only four when applying stricter selection criteria —comparable to those used in GH (Figure 8b). Another interesting observation is the effect of a large number of studies with $N < 10$ near 20°N (triangles in Figure 9). These locations probably cause the anomalous nonzero inclination anomaly in latitude bin 20–30°N (Figures 8c and 8f). This analysis suggests that non-GAD field structure previously observed in the midlatitudes of the Northern Hemisphere (e.g., Cromwell et al., 2018) might be an artifact caused by inclusion of poor-quality data in global lava flows compilation and should be further and carefully examined.

6. Summary and Conclusions

We report here new paleomagnetic data from the GH plateau (32.6–33.2°N, 35.6–35.9°E) spanning the past 5 My. The data set consists of paleomagnetic means from 91 lava flows sites, 51 sampled and analyzed in this study and 40 sampled and analyzed in the 1990s. The chronology of the lava flows is constrained by 57 $^{40}Ar/^{39}Ar$ ages, 39 from previous studies and 18 from this study, which together cover the entire GH plateau. Owing to the large number of paleomagnetic sites we are able to apply fairly strict selection criteria of $k \geq 100$ and $n \geq 5$. The Plio-Pleistocene paleomagnetic pole of the GH, 86.3°N, 120.8°E, $A_{95} = 4.4°$, $k = 25$, $N = 44$ is in agreement with GAD model. The inclination anomaly calculated by averaging paleomagnetic directions is negligible ($\Delta I = -0.4°$) and smaller than predicted by global models and global compilations. Examination of the global data from the PSV10 compilation using different calculation methods and selection criteria show that averaged inclination anomaly values in the global field can be affected by (1) inclusion of poor quality data, (2) zonal averaging scheme by latitude bins, and (3) different approaches to inclination anomaly calculations. We suggest that the large inclination anomaly and non-GAD field structure previously presumed for Northern Hemisphere midlatitudes are not sufficiently robust and should be further and carefully examined.

Acknowledgments
This study was supported by Israel Science Foundation Grant 1364/15 to R. S. and Ministry of National Infrastructure, Energy, and Water Resources Grant 215-17-024 to R. S., and National Science Foundation Grants EAR1345003 and EAR1547263 to L. T. We thank Vitaly Gutkin from the Hebrew University Center for Nanoscience and Nanotechnology for his help with the SEM. We thank the Neev Center for Geoinformatics in the Hebrew University of Jerusalem for use of the computers, software, and working hub. We thank two anonymous reviewers for their constructive comments. We thank Pavel V. Doubrovine for a thorough review and for suggestions that significantly improved the manuscript. The entire data set with our interpretations can be found in the MagIC online data repository at https://earthref.org/MagIC/16676.

References

Biggin, A. J., van Hinsbergen, D. J., Langereis, C. G., Straathof, G. B., & Deenen, M. H. (2008). Geomagnetic secular variation in the Cretaceous Normal Superchron and in the Jurassic. *Physics of the Earth and Planetary Interiors*, *169*(1-4), 3–19. https://doi.org/10.1016/j.pepi.2008.07.004

Cox, A. (1969). Confidence limits for the precision parameter κ. *Geophysical Journal International*, *17*(5), 545–549. https://doi.org/10.1111/j.1365-246X.1969.tb00257.x

Cox, A. (1970). Latitude dependence of the angular dispersion of the geomagnetic field. *Geophysical Journal International*, *20*(3), 253–269. https://doi.org/10.1111/j.1365-246X.1970.tb06069.x

Creer, K. M. (1983). Computer synthesis of geomagnetic paleosecular variations. *Nature*, *304*(5928), 695–699. https://doi.org/10.1038/304695a0

Cromwell, G., Johnson, C. L., Tauxe, L., Constable, C. G., & Jarboe, N. (2018). PSV10: A global data set for 0–10 Ma time-averaged field and paleosecular variation studies. *Geochemistry, Geophysics, Geosystems*, *19*, 1533–1558. https://doi.org/10.1002/2017GC007318

Feraud, G., York, D., Hall, C. M., Goren, N., & Schwarcz, H. P. (1983). $^{40}Ar/^{39}Ar$ age limit for an Acheulian site in Israel. *Nature*, *304*(5923), 263–263, 265. https://doi.org/10.1038/304263a0

Fisher, R. A. (1953). Dispersion on a sphere. *Proceedings of the Royal Society of London A*, *217*(1130), 295–305. https://doi.org/10.1098/rspa.1953.0064

Gee, J. S., & Kent, D. V. (2007). Source of oceanic magnetic anomalies and the geomagnetic polarity timescale. In M. Kono, & G. Schubert (Eds.), *Treatise on Geophysics* (Vol. 5, pp. 455–507). Amsterdam ; Boston: Elsevier. https://doi.org/10.1016/B978-044452748-6/00097-3

Heimann, A., & Ron, H. (1993). Geometrical changes of plate boundaries along part of the of the northern Dead Sea transform: geochronologic and paleomagnetic evidence. *Tectonics*, *12*(2), 477–491. https://doi.org/10.1029/92TC01789

Heimann, A., Steinitz, G., Mor, D., & Shaliv, G. (1996). The Cover Basalt Formation, its age its regional tectonic setting: Implications from K-Ar and $^{40}Ar/^{39}Ar$ geochronology. *Israel Journal of Earth Sciences*, *45*, 55–71.

Hurwitz, S., Matmon, A., & Heimann, A. (2000). Deformation along the margins of the Dead Sea Transform: The Yehudiyya Block, Golan Heights. *Israel Journal of Earth Sciences*, *48*, 257–264.

Inbar, M., Gilichinsky, M. (2009). New Ar-Ar dates from lava flows and cinder cones in the Golan Heights—Some geomorphic implications. *Israel Geological Society Meeting, Kfar Blum, Israel*.

Johnson, C. L., & Constable, C. G. (1996). Paleosecular variation recorded by lava flows over the last 5 Myr. *Philosophical Transactions of the Royal Society of London, Series A*, *354*, 89–141.

Johnson, C. L., Constable, C. G., Tauxe, L., Barendregt, R., Brown, L. L., Coe, R. S., et al. (2008). Recent investigations of the 0–5 Ma geomagnetic field recorded by lava flows. *Geochemistry, Geophysics, Geosystems*, *9*, Q04032. https://doi.org/10.1029/2007GC001696

Johnson, C. L., & McFadden, P. L. (2015). The time-averaged field and paleosecular variation. In M. Kono (Ed.), Geomagnetism; G. Schubert (Ed.), *Treatise on geophysics* (2nd ed., Vol. 5, pp. 385–417). Amsterdam, The Netherlands: Elsevier. https://10.1016/B978-0-444-53802-4.00105-6

Kirschvink, J. L. (1980). The least-squares line and plane and the analysis of paleomagnetic data. *Royal Astronomical Society*, *62*(3), 699–718. https://doi.org/10.1111/j.1365-246X.1980.tb02601.x

Koppers, A. (2003). High-resolution $^{40}Ar/^{39}Ar$ dating of the oldest oceanic basement basalts in the western pacific basin. *Geochemistry, Geophysics, Geosystems*, *4*(11), 8914. https://doi.org/10.1029/2003GC000574

Koppers, A., Gowen, M., Colwell, L., Gee, J. S., Lonsdale, P., Mahoney, J. J., & Duncan, R. A. (2011). New $^{40}Ar/^{39}Ar$ age progression for the Louisville hot spot trail and implications for inter-hot spot motion. *Geochemistry, Geophysics, Geosystems*, *12*, Q0AM02. https://doi.org/10.1029/2011GC003804

Koppers, A., Russell, J., Jackson, M., Konter, J., Staudigel, H., & Hart, S. (2008). Samoa reinstated as a primary hotspot trail. *Geology*, *36*(6), 435–438. https://doi.org/10.1130/G24,630A.1

Koppers, A., Russell, J., Roberts, J., Jackson, M., Konter, J., Wright, D., et al. (2011). Age systematics of two young en echelon samoan volcanic trails. *Geochemistry, Geophysics, Geosystems*, *12*, Q07025. https://doi.org/10.1029/2010GC003438

Koppers, A., & Staudigel, H. (2005). Asynchronous bends in Pacific seamount trails: A case for extensional volcanism. *Science*, *307*(5711), 904–907. https://doi.org/10.1126/science.1107260

Koppers, A., Staudigel, H., Wijbrans, J., & J. (2000). Dating crystalline groundmass separates of altered Cretaceous seamount basalts by the $^{40}Ar/^{39}Ar$ incremental heating technique. *Chemical Geology*, *166*(1-2), 139–158. https://doi.org/10.1016/S0009-2541(99)00188-6

Lee, S. (1983). A study of the time-averaged paleomagnetic field for the past 195 million years, Ph. D Thesis, *The Australian National University, Canberra, ACT, Australia*.

McElhinny, M. W., & McFadden, P. L. (1997). Palaeosecular variation over the past 5 Myr based on a new generalized database. *Geophysical Journal International*, *131*(2), 240–252. https://doi.org/10.1111/j.1365-246X.1997.tb01219.x

McElhinny, M. W., & Merrill, R. T. (1975). Geomagnetic secular variation over the past 5 My. *Reviews of Geophysics*, *13*(5), 687–708. https://doi.org/10.1029/RG013i005p00687

Meiler, M. (2011). The deep geological structure of the Golan Heights and the evolution of the adjacent Dead Sea fault system: PhD thesis, *Tel Aviv University, Tel Aviv, Israel*.

Michelson, H., & Mor, D. (1985). The geological map of Israel, Gamla. *Geological Survey of Israel*, scale 1:50,000.

Mor, D. (1986). The volcanism of the Golan Heights. *Geological Survey of Israel*, Report GSI/5/86, 155p. (in Hebrew with English abstract).

Mor, D. (1987a). The geological map of Israel, Har Odem. *Geological Survey of Israel*, sheet 2-II, scale 1:50,000, 1 sheet.

Mor, D. (1987b). The geological map of Israel, Qazrin. *Geological Survey of Israel*, sheet 2-II, scale 1:50,000, 1 sheet.

Mor, D. (1993). A time-table for the Levant volcanic province, according to K-Ar dating in the Golan heights, Israel. *Journal of African Earth Sciences*, *16*(3), 223–234. https://doi.org/10.1016/0899-5362(93)90044-Q

Quidelleur, X., Valet, J.-P., Courtillot, V., & Hulot, G. (1994). Long-term geometry of the geomagnetic field for the last five million years: An updated secular variation database. *Geophysical Research Letters*, *21*(15), 1639–1642. https://doi.org/10.1029/94GL01105

Ron, H., Freund, R., Garfunkel, Z., & Nur, A. (1984). Block rotation by strike-slip faulting: structural and paleomagnetic evidence. *Journal of Geophysical Research*, *89*(B7), 6256–6270. https://doi.org/10.1029/JB089iB07p06256

Ron, H., Heimann, A., & Garfunkel, Z. (1992). Pliocene paleomagnetic pole of the Arabian plate: implications for the Levant plate kinematics, *IPRG Report* 889/388/90.

Shaanan, U., Porat, N., Navon, O., Weinberger, R., Calvert, A., & Weinstein, Y. (2010). OSL dating of a Pleistocene maar: Birket Ram, the Golan heights. *Journal of Volcanology and Geothermal Research*, *201*(1-4), 397–403. https://doi.org/10.1016/j.jvolgeores.2010.06.007

Sneh, A., & Weinberger, R. (2003). Geological map of Israel. Sheet 2-II Metulla, scale 1:50000, *Geological Survey of Israel*.

Sneh, A., & Weinberger, R. (2006). Geological map of Israel. Sheet 2-IV Rosh Pinna, scale 1:50000, *Geological Survey of Israel*.

Tauxe, L., Constable, C., Johnson, C. L., Koppers, A. A. P., Miller, W. R., & Staudigel, H. (2003). Paleomagnetism of the southwestern U.S.A. recorded by 0–5 Ma igneous rocks. *Geochemistry, Geophysics, Geosystems*, *4*(4), 8802. https://doi.org/10.1029/2002GC000343

Tauxe, L., & Kent, D. V. (2004). A simplified statistical model for the geomagnetic field and the detection of shallow bias in paleomagnetic inclinations: Was the ancient magnetic field dipolar? In J. E. T. Channell, D. V. Kent, W. Lowrie, & J. G. Meert (Eds.), *Timescales of the paleomagnetic field* (Vol. 145, pp. 101–116). Washington, DC: American Geophysical Union.

Tauxe, L., Kylstra, N., & Constable, C. (1991). Bootstrap statistics for paleomagnetic data. *Journal of Geophysical Research*, *96*(B7), 11723–11,740. https://doi.org/10.1029/91JB00572

Tauxe, L., & Staudigel, H. (2004). Strength of the geomagnetic field in the Cretaceous Normal Superchron: New data fromsubmarine basaltic glass of the Troodos Ophiolite. *Geochemistry Geophysics, Geosystems*, *5*, Q02H06. https://doi.org/10.1029/2003GC000635

Tauxe, L., Shaar, R., Jonestrask, L., Swanson-Hysell, N. L., Jarboe, N., Minnett, R., et al. (2016). PmagPy: Software package for paleomagnetic data analysis and a bridge to the Magnetics Information Consortium (MagIC) Database. *Geochemistry, Geophysics, Geosystems*, *17*, 2450–2463. https://doi.org/10.1002/2016GC006307

Vandamme, D. (1994). A new method to determine paleosecular variation. *Physics of the Earth and Planetary Interiors*, *85*(1-2), 131–142. https://doi.org/10.1016/0031-9201(94)90012-4

Weinstein, Y., Navon, O., Altherr, R., & Stein, M. (2006). The role of fluids and of lithospheric heterogeneity in the generation of alkali basaltic suites from northwestern Arabia. *Journal of Petrology*, *47*(5), 1017–1050. https://doi.org/10.1093/petrology/egl003

Weinstein, Y., Weinberger, R., & Calvert, A. (2013). High-resolution $^{40}Ar/^{39}Ar$ study of Mount Avital, northern Golan: Reconstructing the interaction between volcanism and a drainage system and their impact on eruptive styles. *Bulletin of Volcanology*, *75*(5), 712. https://doi.org/10.1007/s00445-013-0712-7

Wilson, R. L. (1970). Permanent aspects of the Earth's nondipole magnetic field over Upper Tertiary times. *Geophysical Journal of the Royal Astronomical Society*, *19*(4), 417–437. https://doi.org/10.1111/j.1365-246X.1970.tb06056.x

Zijderveld, J. D. A. (1967). A.C. demagnetization in rocks: analysis of results. In D. W. Collinson, K. M. Creer, & S. K. Runcorn (Eds.), *Methods in Paleomagnetism* (pp. 254–286). New York: Elsevier.